Inkjet-printed electrochemically reduced graphene oxide microelectrode as a platform for HT-2 mycotoxin immunoenzymatic biosensing

Jiri Kudr [a, b]***, Lei Zhao*** [a, c]***, Emily P. Nguyen*** [a]***, Henri Arola*** [d]***, Tarja K. Nevanen*** [d]***, Vojtech Adam*** [b, e]***, Ondrej Zitka*** [b, e]***, Arben Merkoçi*** [a, f,*]

[a] *Catalan Institute of Nanoscience and Nanotechnology (ICN2), CSIC and The Barcelona Institute of Science and Technology, Bellaterra, ES-08193, Spain*

[b] *Department of Chemistry and Biochemistry, Mendel University in Brno, Zemedelska 1, Brno, CZ-613 00, Czech Republic*

[c] *Department of Chemical Engineering, School of Engineering, UAB, Bellaterra, ES-08193, Spain*

[d] *VTT Technical Research Centre of Finland, Espoo, FI-02150, Finland*

[e] *Central European Institute of Technology, Brno University of Technology, Brno, CZ-616 00, Czech Republic*

[f] *ICREA – Institucio Catalana de Recerca i Estudis Avançats, Barcelona, ES-08010, Spain*

*Corresponding author. E-mail: arben.merkoci@icn2.cat (Arben Merkoçi)

ABSTRACT

The design and application of an inkjet-printed electrochemically reduced graphene oxide microelectrode for HT-2 mycotoxin immunoenzymatic biosensing is reported. A water-based graphene oxide ink was first formulated and single-drop line working microelectrodes were inkjet-printed onto poly(ethylene 2,6-naphthalate) substrates, with dimensions of 78 μm in width and 30 nm in height after solvent evaporation. The printed graphene oxide microelectrodes were electrochemically reduced and characterized by Raman and X-ray photoelectron spectroscopy spectroscopies in addition to microscopies. Through optimization of the electrochemical reduction parameters, differential pulse voltammetry were performed to examine the sensing of 1-naphthol (1-N), where it was revealed that

reduction times had significant effects on electrode performance. The developed microelectrodes were then used as an immunoenzymatic biosensor for the detection of HT-2 mycotoxin based on carbodiimide linking of the microelectrode surface and HT-2 toxin antigen binding fragment of antibody (anti-HT2 (10) Fab). The HT-2 toxin and anti-HT2 (10) Fab reaction was reported by anti-HT2 immune complex single-chain variable fragment of antibody fused with alkaline phosphatase (anti-IC-HT2 scFv-ALP) which is able to produce an electroactive reporter – 1-N. The biosensor showed detection limits of 1.6 $ng \cdot mL^{-1}$ and a linear dynamic range of 6.3 – 100.0 $ng \cdot mL^{-1}$ within a 5 minute incubation with 1-naphthyl phosphate (1-NP) substrate.

1. Introduction

Graphene is a carbon allotrope comprising of a single layer of carbon atoms arranged in a honeycomb lattice structure. The oxygen content in graphene-based materials play an important role in the field of electrochemistry, as it significantly decreases the material´s conductivity (Benchirouf et al. 2016; Chen et al. 2011). Reduced graphene oxide (RGO) represents the transition material – possesses good heterogeneous electron transfer rate but still enough oxygen groups that can facilitate functionalization (Ren et al. 2017). Electrochemical reduction of graphene oxide is a fast, simple and economic alternative approach to other conventional chemical reduction methods, which typically involve the use of toxic reducing agents and can lead to contamination of the resulting material. Furthermore, electrochemical reduction methods can be easily adapted for applications where thermal reduction is not possible, for example reduction of structures on plastic substrates (Toh et al. 2014).

Traditionally, electronic devices fabricated by photolithography suffer from several disadvantages such as complicated assembly processes, expensive instrumentation and use of harmful chemicals. Inkjet printing (IJP) is a promising alternative technique for the production of advanced future electronic devices as it allows for direct (no template) and non-contact printing onto flexible substrates such as

plastics, nanocellulose, and wearable e-textiles (Hermerschmidt et al. 2018; Hoeng et al. 2017; Karim et al. 2017). Depending on the capabilities of the printer, even deposition of functional materials with extraordinary precision can be achieved (Bachmann et al. 2017). Due to these outstanding properties, IJP is not only a suitable choice for graphics, but also for printing of semi-conductive and/or insulating materials for thin-film transistors, electrochemical sensors, and wearable electronics (da Silva et al. 2014; Medina-Sanchez et al. 2014; Zhan et al. 2017). Furthermore, IJP has the added advantage for ease of mass production of small, disposable, low cost electrochemical biosensors. Depending on the intended application, the selection of conductive material(s) is mainly determined by the desired conductivity, optical transparency and bending stability (especially important for flexible electronics) (He and Derby 2017; Kamyshny and Magdassi 2014). Typically, metal-based inks, such as Au or Ag nanoparticle solutions, are used as standard materials for IJP to fabricate conductive tracks (Su et al. 2019; Zikulnig et al. 2019). Recently, the incorporation of 2D materials for IJP has been considered as an alternative for some applications, because metallic nanoparticles based inks are expensive, tend to oxidize and require high-temperature post-printing sintering (Bonaccorso et al. 2016; Park et al. 2007; Singh et al. 2010). Moreover, Ag and Cu nanoparticles used for the conductive ink formulations are not stable in the most common solvents such as water, ethanol or acetone (Dearden et al. 2005; Park et al. 2007). Although the characteristics of IJP graphene-based platforms cannot compete with the high conductivity, deposition control and optical transparency of chemically deposited graphene, it has nonetheless attracted attention of researchers worldwide (Bonaccorso et al. 2016; Singh et al. 2010). One of the primary challenges of printing with pristine graphene is the tendency of the material to aggregate, leading to low ink stability and printhead nozzles clogging (Michel et al. 2017). To overcome this, one approach is to benefit from exfoliated GO as a source material, since oxygen-containing groups of GO enables its dispersion in water-based inks. These inks can create continuous films over desired substrates and a conductive film can be obtained using post-printing reduction (Pei and Li 2017).

With respect to agro-economics and the impact on global agriculture, the HT-2 toxin, produced by different *Fusarium* species, is a member of the group of the most relevant mycotoxins (Hussein and Brasel 2001). HT-2 can contaminate small grain cereals and maize in the field, but also during wet storage and inappropriate transport. It has been shown that HT-2 toxin is only partially degraded during thermal food processing (Kuchenbuch et al. 2018). Causing apoptosis and inhibiting protein synthesis, HT-2 is contaminant of concern to human and animal health (Yang et al. 2017). According to a Recommendation of The European Commission, in cases of analytical screening techniques the limit of detection should not exceed 25 $\mu g \cdot kg^{-1}$ for the sum of HT-2 and T-2 toxin (EC 2013). Common levels of toxins in contaminated grains for human consumption and breakfast cereals were reaching from tens to hundreds of $\mu g \cdot kg^{-1}$ (Kaukoranta et al. 2019).

In this paper, we present the development of an ink, based on GO, and demonstrate its compatibility for inkjet printing by fabricating electrodes where the working microelectrodes were formed *via* inkjet printing. After optimization of the reduction parameters, we obtained electrochemically reduced graphene oxide (ERGO) microelectrodes and the performance was evaluated by differential pulse voltammetry (DPV) for the sensing of 1-naphthol (1-N). The results indicated that the ERGO microelectrodes were suitable for biosensing and their application was demonstrated as an enzymatic immunosensor for the detection of HT-2 mycotoxin.

2. Materials and methods

2.1. Chemicals

Ethylene glycol (EG), sodium dodecyl sulfate (SDS), 1-NP monosodium salt, 1-N, diethanolamine (DEA), n-hydroxysuccinimide (NHS), n-(3-dimethylaminopropyl)-n-ethylcarbodiimide hydrochloride (EDC), 2-(N-Morpholino)ethanesulfonic acid (MES) and other chemicals were purchased from Sigma-Aldrich (St. Louis, MO, USA) in ACS purity and were used as received. All water-based solutions were

prepared using milli-Q water (resistivity higher than 18.2 $M\Omega \cdot cm^{-1}$ at 25 °C) from Millipore (Burlington, MA, USA).

2.2. Fabrication of electrode

Poly(ethylene 2,6-naphthalate) (PEN, 0.075 mm thickness, Goodfellow, Huntingdon, UK) substrate was cleaned using atmospheric-pressure oxygen plasma for 30 min (Harrick Plasma, Ithaca, NY, USA), followed by soaking in 1M NaOH bath for 30 min at 25 °C, then washed with water and dried with compressed air flow. The counter electrodes and graphite tracks of working electrodes were screen-printed using carbon sensor paste (C2030519P4, Gwent Group, Pontypool, UK). Pseudoreference electrodes were printed using Ag/AgCl paste (C61003P7, Gwent Group, Pontypool, UK). The electrodes were cured at 120 °C for 30 min in an oven (JP Selecta, Barcelona, Spain).

40 mL of single layer GO water solution (N002-PS-1.0, Angstron Materials, Dayton, OH, USA) of concentration 1 wt% was sonicated for 2 h (80 % amplitude, 1 s pulse, 1 s pause, cooling temperature 15 °C, protecting temperature 40 °C) using an ultrasonicator equipped with a 1000 W sonic head and a water cooling system (Col-Int TECH, Irmo, SC, USA). To create the ink, 600 mg of the GO solution was added to 3.6 mL of milli-Q water, 6 mg of SDS and 1.8 mL of EG and mixed using a Q125 probe sonicator (Qsonica, Melville, NY, USA) with the following settings: time 300 s, amplitude 100 %, pulse 2 s, pause 1 s. The solution was cooled using an ice bath during sonication. The ink was obtained by filtering with cellulose acetate syringe filter (0.45 μm cut-off, VWR, Radnor, PA, USA).

The GO working electrodes were printed using a Dimatix Materials Printer DMP-2850 (Fujifilm, Minato, Japan) with a DMC-11610 printhead dispensing 10 pL nominal drop volume (nozzle diameter of 21 μm). The printhead and substrate plate were set to 35 °C. A single nozzle with continuous jetting was used to print 10 mm-long working electrodes. Each line was printed 30-times with 30 s pauses between individual layers and drop-spacing of 30 μm. The dispersion was printed at a voltage of 11 V

with a frequency of 5 kHz. A custom waveform profile was used for the GO ink printing. The distance between the printhead and substrate was set to 500 μm.

Prior to reduction of the GO, the electrodes were treated at 120 °C for 2 hours. Then, 50 μL of KCl solution in milli-Q water was pipetted onto the electrode to cover the pseudoreference electrode, counter electrode and the whole GO strip, including the undefined part of the graphite carbon working electrode track. The reduction was performed using chronopotentiometry at −1.5 V. After the reduction, the electrodes were washed with milli-Q water, dried with compressed air and the insulating line (Dielectric ink D2070423P5, Gwent Group, Pontypool, UK) was added to prevent solutions from having contact with the graphite part of the working electrode. Finally, the electrodes were treated at 200 °C for 5 min.

2.3. Biosensor fabrication

Anti-HT2 (10) Fab was attached to the ERGO microelectrode *via* EDC/NHS linker chemistry. In detail, after the electrodes were briefly washed with MES buffer (pH 6), a 30 μL drop of EDC/NHS solution (0.1 M, in MES buffer) was added onto the printed area and left to incubate at room temperature for 30 min. The electrodes were then thoroughly washed with MES buffer to remove any excess EDC/NHS and 10 μL of anti-HT2 (10) Fab (typically 10 $\mu g \cdot mL^{-1}$, in phosphate buffered saline (PBS) pH 6.5) was added onto the electrode and incubated for another 30 min. The drop was then removed and 30 μL of Tris buffer (pH 8) was added onto the electrode for 30 min. Subsequently, 30 μL of blocking buffer (2 % bovine serum albumine in PBS pH 7.4 with 0.05 % tween-20) was pipetted onto the electrode and incubated for 30 min. The electrodes were washed twice with washing buffer (PBS pH 7.4 with 0.05 % tween-20) and samples containing the mycotoxin (30 μL total volume, diluted in blocking buffer in 1:1 ratio, 30 min incubation) were added. The electrodes were then washed thoroughly with washing buffer and dried at 25 °C. Anti-IC-HT2 scFv-ALP was then added for 30 min and then removed with washing buffer. Analysis was performed by addition of 5 mM 1-NP dissolved in 0.1 M DEA buffer (pH 9.8 containing 1 mM $MgCl_2$). After 5 min of incubation with 1-NP, DPV electrochemical analysis was

performed using the following settings: initial potential −0.8 V, end potential 0.7 V, speed of polarization 0.5 mV · s^{-1}, modulation amplitude 175 mV, modulation time 10 ms, interval time 1 s, no deposition or conditioning potential was set.

2.4. Biological materials

Anti-HT2 (10) Fab and anti-IC-HT2 ScFv-ALP fusion antibody were provided by VTT (Espoo, Finland) (Arola et al. 2017). HT-2 toxin (15-Acetoxy-3α,4β-dihydroxy-8α-(3-methylbutyryloxy)-12,13-epoxytrichothec-9-ene) was bought from Sigma-Aldrich (St. Louis, MO, USA). The content of a whole vial of the mycotoxin was dissolved in dimethyl sulfoxide (1 mg · mL^{-1}) to create the stock solution. Individual HT-2 concentrations were obtained by dilution. Gibco One Shot Fetal bovine serum (Thermo Fisher Scientific, Waltham, MA, USA) was used as a matrix for real sample analysis.

2.5. Electrode effective surface calculation

In order to determine the electroactive area of the ERGO microelectrode, cyclic voltammograms (CV) were obtained using 1 mM $[Fe(CN)_6]^{3-}$/$[Fe(CN)_6]^{4-}$ redox probe in 0.1 M KCl. The electroactive surface was calculated according to Randles-Sevcik equation for reversible electrode process:

$$Ip = 2.69 \cdot 10^5 \cdot A \cdot D^{1/2} \cdot n^{3/2} \cdot v^{1/2} \cdot C \qquad \text{Eq. (1)}$$

where I_p is anodic current peak (A), A is the electroactive area (cm^2), D is the diffusion coefficient of $[Fe(CN)_6]^{4-}$ in solution and is $6.1 \cdot 10^{-6}$ $cm^2 \cdot s^{-1}$, n is the number of electrons transferred in half-reaction (1 in case of $[Fe(CN)_6]^{4-}$), v is scan rate (0.1 V · s^{-1} was chosen) and C is $[Fe(CN)_6]^{4-}$ concentration (mol · L^{-1}).

2.6. Instrumentation

For characterization of the materials and the electrodes, Magellan 400 L field emission scanning electron microscope (SEM, FEI, Hillsboro, OR, USA), EasyDrop Contact Angle Measuring instrument (Kruss,

Hamburg, Germany), optical microscope (Olympus1X71, Olympus, Tokyo, Japan) were used. Asylum MFP-3D atomic force microscope (AFM) (Oxford Instruments, Abingdon, UK) was used for electrode characterization. Bruker Dimension FastScan atomic force microscope (Bruker Nano Surface, Santa Barbara, CA, USA) operated in tapping mode was used for GO characterization. X-ray photoelectron spectroscopic (XPS) measurements were performed at room temperature with a SPECS PHOIBOS 150 hemispherical analyzer (SPECS GmbH, Berlin, Germany) in a base pressure of $5 \cdot 10^{-10}$ mbar using monochromatic Al K-alpha radiation (1486.74 eV) as an excitation source. XPS spectra were then evaluated using Fityk sofware. Raman spectra were obtained using a confocal Raman microscope alpha300r equipped with a 488 nm laser (WITec, Ulm, Germany) and parameters of 1.5 mW laser power, grating of 600 $g \cdot nm^{-1}$, objective 50x, exposure of 10 s and 3 accumulations for every single spectra. For electrochemical measurements, an Autolab PGSTAT 302 (Metrohm, Herissau, Switzerland) equipped with frequency response analyzer PGST30 was used. CV and DPV were evaluated using GPES electrochemical software. EIS spectra, including equivalent circuit elements calculations, were evaluated using NOVA (both Metrohm, Herissau, Switzerland).

3. Results and discussion

Commercial GO was utilized as the main component within the ink. Prior to ink formulation the GO stock solution, containing 1 wt% of GO, was thoroughly sonicated. The dense black GO solution was then mixed and sonicated with EG, water and SDS to obtain the GO water-based ink containing 1 $mg \cdot mL^{-1}$ GO (0.1 wt%), 30 % EG and 1 $mg \cdot mL^{-1}$ SDS. It is recommended for materials sizes to be less than $1/100^{th}$ the size of nozzle, to avoid obstruction of the printhead nozzle and guarantee successful printing. To ensure that the GO sheets were of suitable dimensions, the GO sheets were initially treated to intense continuous sonication and then filtered to remove the undesired sizes. Figure 1(a) is an SEM micrograph of the ink and indicates that the GO collected after the formulation procedure was within the lateral ranges of 226 – 875 nm. Compared to source GO, the lateral diameter of treated GO significantly

decreased after sonication (see Fig. S1 for comparison). It is well-known that sonication induces fragmentation of the GO sheets and can create crystal structure defects, which are important for heterogeneous electron transfer (HET) in electrochemistry (Ye and Feng 2016; Zhong et al. 2014). Further, the presence of single-layer GO sheets within stock solution provided by manufacturer was confirmed by atomic force microscopy (AFM). The obtained data showed the graphene oxide thickness of about 1 nm (Fig. S2). In accordance with previously published articles, the used graphene oxide can be interpreted as single-layer sheets (Bartlam et al. 2018; Paredes et al. 2009; Stankovich et al. 2006). As the viscosity of water is too low and the surface tension is too high to be used for IJP, EG was added as a rheology modifier and humectant, while SDS was added to adjust the ink ’s surface tension (Li et al. 2018; Vaseem et al. 2012). Printing resolution and homogeneity of printed design are influenced by droplet spread and are attributed to the wettability of the ink with respect to the substrate (Stringer and Derby 2009). Both surface chemistry and roughness contribute to the wettability effects of substrate. Since the droplets produced in IJP are very small (10 pL in our case) there are high demands for substrate quality. As a substrate for electrode printing, we have selected transparent and flexible PEN suitable for development of wearable electrode sensors (Shiwaku et al. 2018). The substrate was treated with atmospheric-pressure oxygen plasma in combination with chemical hydrolysis prior to printing. As reported by Gonzales *et al.* (Gonzalez et al. 2008), plasma treatment of PEN can induce oxidation of the aromatic rings of the polymer chains. After the plasma treatment, the substrate was rinsed with NaOH to increase the substrate roughness (Cammarano et al. 2013). Figure 1(b) and 1(c) shows a decrease of the contact angle of the droplet upon plasma and NaOH treatment of the substrate, indicating that the wettability of the substrate was improved after such treatments.

The printing of the electrochemical sensor was performed using various types of printing techniques. The counter electrodes, pseudoreference electrodes and the working electrodes tracks were printed using traditional screen printing techniques. The active area of the working electrode was inkjet-printed using the developed GO ink, ensuring that a small section of the area was overlapping with the screen printed

track to enable its electrochemical activity. An SEM micrograph of the whole electrode can be seen in Fig. S2. Following the reduction step, an insulating layer was added to cover the entire working electrode graphitic parts and to define the active surface of electrodes. Scheme of ERGO microelectrodes main fabrication steps can be seen in Fig. 1(d).

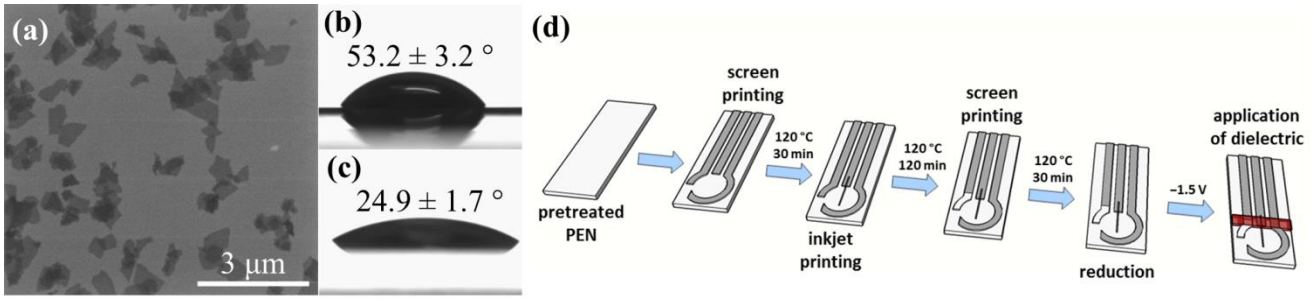

Fig. 1. (a) SEM micrograph of GO flakes contained in ink. (b) Contact angle for droplet of IJP ink on non-treated and (c) treated PEN substrate. (d) Scheme of ERGO microelectrode fabrication.

3.1. ERGO microelectrode characterization

An optical microscope image of the working electrode track and the GO printed active area interface is presented in Fig. 2(a). The large dark feature in the upper left is the end of the screen-printed working electrode (WE) track, while a continuous strip of GO can be seen as a narrow grey line. The printed GO strip exhibits well-defined edges with a width of 78 µm. As thermal reduction of the GO strip was not possible, due to potential damages to the PEN substrate, an electrochemical approach was adopted for the reduction of the GO active area to ERGO. The electrochemical reduction was performed in 3 mM KCl solution at a potential of −1.5 V *vs.* Ag/AgCl. As reported elsewhere, successful reduction was visually observed by a color change of the GO from light brown to light black (Fig. 1(b)) (Kudr et al. 2016). The reduction of GO to ERGO was also confirmed using Raman spectroscopy by observation of the two characteristic D and G bands of graphene-based materials. It has been reported that the D band is closely related to the degree of defects and disorder within the hexagonal lattice and should not be observed in the case of pristine graphene, like that grown by chemical vapor deposition (Juang et al. 2010). Conversely, the G band corresponds to the in-plane vibrations of sp^2 carbon atoms of graphene

lattice and thus increases with reduction of C-O/C=O. As such, in the case of ERGO, the ratio of these peak intensities (I_D/I_G) are often used to survey the level of oxidation of graphene-based materials (Ramesha and Sampath 2009). In both our samples of GO and ERGO, the D and G bands were observed at 1354 cm^{-1} and 1578 cm^{-1}, respectively (Fig. 1(c)) and without any shifts upon comparison of the before and after spectra. However, the intensities of these peaks show obvious variations and suggest successful electrochemical reduction of the GO to ERGO as the I_D/I_G ratio increased from 0.90 to 1.25. Furthermore, this observation also suggests an increase of lattice-defects during the reduction process and is in good agreement with previous studies (Kuang et al. 2018). Since the procedure of electrodes fabrication included thermal treatment, Raman spectra of a thermally treated working electrode were obtained as a control (see Fig. S3 for comparison). The ERGO electrodes were also characterized using XPS to determine the chemical states of carbon and oxygen (Fig. 1(d)). Shirley background subtraction and fitting with Voigt function (convolution of Gaussian and Lorentzian peak shapes) were performed. Upon evaluation of the C1s spectrum, the carbon peak was deconvoluted to 5 individual peaks: C-C sp^2 (284.5 eV), C-OH (285.5 eV), C-O (286.4 eV), C=O (287.6 eV) and O-C=O (289.9 eV) (Casero et al. 2014; Casero et al. 2013). Four distinguishable oxygen containing peaks were observed in the O1s spectrum (C=O at 530.7 eV, O-C=O at 532.2 eV, OH at 533.1 eV and C-O-C at 533.7 eV). It demonstrates that even after electrochemical reduction, carboxyl functional groups which will facilitate covalent attachment of antibodies to electrode were still presented within ERGO electrodes (Raj and John 2013). AFM height profile suggests that the ERGO strip electrode goes 30 nm above the PEN substrate (Fig. 1(e)). Given that the intrinsic thickness of GO is 1 nm we can conclude that the electrode strip was created by around 30 layered sheets of ERGO (Zhang et al. 2010). An AFM phase image of the electrode and substrate borderline can be seen in Fig. S4.

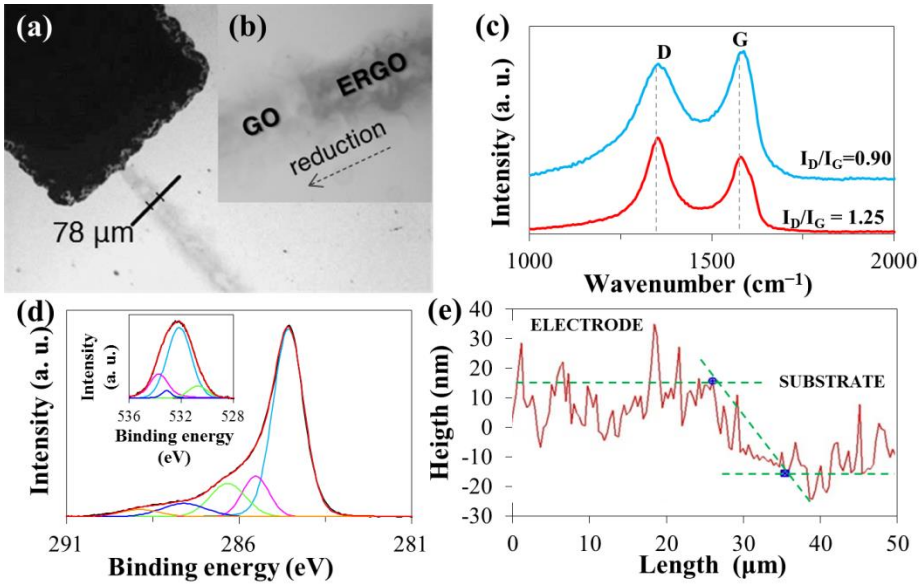

Fig. 2. (a) Optical microscope image of IJP GO strip electrode before reduction and (b) during reduction. (c) Raman spectra of GO electrode before reduction step (blue line) and after electrochemical reduction with thermal treatment (red line). (d) Deconvoluted XPS C 1s and O 1s (inset) spectrum of ERGO. (e) Height profile of ERGO strip electrode obtained by AFM.

3.2. ERGO microelectrode optimization for 1-N sensing

The ERGO microelectrodes were characterized with cyclic voltammetry at varying speeds of polarization. As shown in Fig. 3(a), the ferri/ferrocyanide redox reaction displayed well-defined oxidation and reduction peaks where it can be observed that there is an increase of the current with each increased scan rate. The anion oxidation current of ferrocyanide was plotted against the square root of the scan rates and revealed a linear relationship (Fig. 3(b)), suggesting that there is a diffusion controlled mechanism for the oxidation/reduction of ferro/ferricyanide on the ERGO electrode. However, large shifts of the faradaic peaks which suggested slow electrode kinetics towards oxidation/reduction of the used probe were observed. Brownson *et al.* reported similar behavior for highly ordered pyrolytic graphite electrodes with a single layer of pristine graphene (Brownson et al. 2011). This can be also caused by the oxygen content in ERGO as the ferri/ferrocyanide redox probe is highly sensitive to the oxygen content within the electrode material (Tan et al. 2014). Using Randles-Sevcik equation (Eq. (1))

for reversible electrode process, the electroactive surface of electrode was determined to be 5.2 mm^2 which was by 0.2 mm^2 bigger than the geometrical surface. The influence of KCl concentration in the reduction solution and reduction time was determined based on the sensitivity of the ERGO strip electrode towards sensing of 1-N. These experiments were performed with electrodes fabricated using the same procedure as described for the microelectrodes, but with a 10-times larger geometric surface (1.0 × 5 mm~5 mm^2) of working electrode used to observe the enhanced differences. As is evident from Fig. 3(c), the reduction time of such fabricated GO electrodes influences 1-N sensing. It is consistent with the findings of Feng *et al.*, where they described the electrochemical reduction of graphene oxide as a multi-step process and that the abundance of oxygen-containing groups depended on the reduction time (Feng et al. 2016). It is worth noting that even after 300 s of reduction, at a constant potential of −1.5 V *vs.* Ag/AgCl, the whole printed GO layer was reduced, as indicated by a color change from brown to black. Since the reduction time of 900 s increased the electrochemical signal by 45 ± 5 % (n = 3), we can conclude that the reduction time plays an important role for the sensing of 1-N. Further increase of reduction time to 1200 s enhanced electrode performance negligibly. Regarding GO microelectrodes reduction, a time of 1000 s was normally used but from our experience the reduction process is highly dependent on the quality (homogeneity) of the printed GO strip (drop spacing, number of printed layers and even substrate pretreatment procedure). No significant changes of 1-N signals were observed with varying concentrations of KCl. This suggests that the electrolyte solution had no effect on the performance of the ERGO microelectrode (Fig. 3(d)) and consequently a concentration of 3 mM KCl was chosen for reduction of the GO electrodes.

The dependence of 1-N DPV signal on the modulation amplitude, modulation time and speed of polarization were assessed. The optimal results of these measurements are indicated by a red diamond in Fig. 3(e), (f) and (g). Thus for the DPV measurements, the modulation amplitude was set to 175 mV, modulation time 10 ms and a scan rate of 5 $mV \cdot s^{-1}$ was used. As a last step, the dependence of 1-N oxidation signal at +0.05 V *vs* its concentration in DEA buffer was evaluated. The linear range of the

calibration curve was observed between 31.25 and 0.24 µM concentration with satisfactory factor of determination, $R^2 = 0.994$. It showed that an electrode with settings as described above enabled reliable and sensitive detection of 1-N (Fig. 3(h)).

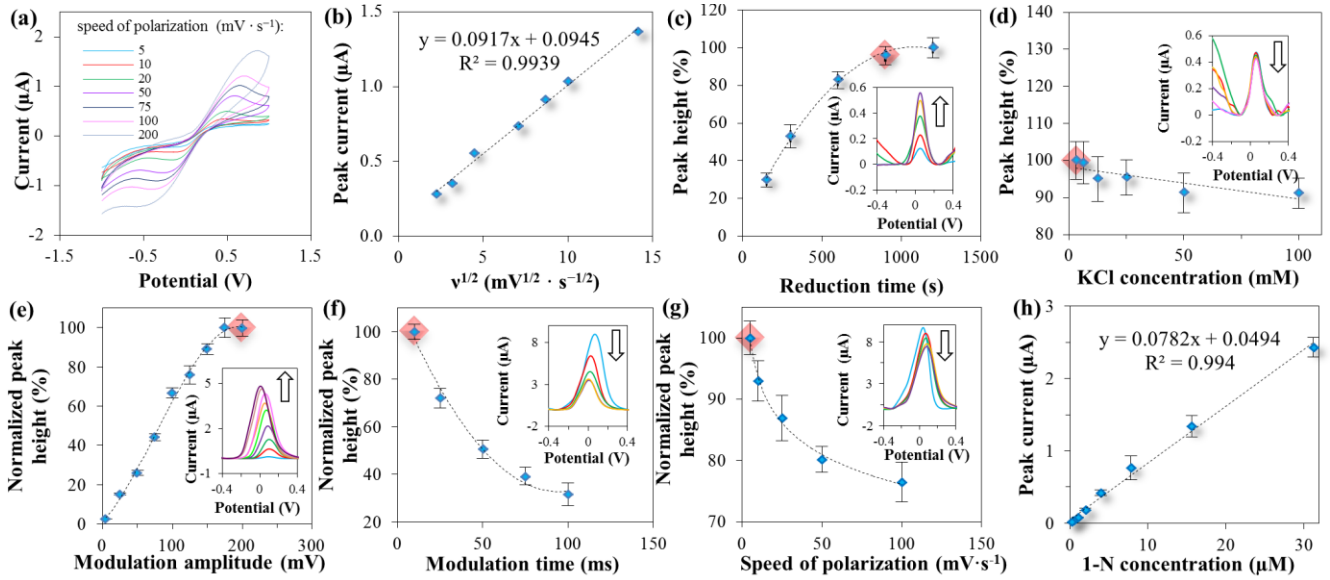

Fig. 3. (a) CV of 1 mM $[Fe(CN)_6]^{3-}/[Fe(CN)_6]^{4-}$ in 0.1 M KCl (5 – 200 mV · s^{-1}) recorded using ERGO microelectrode. (b) The dependence of 1 mM $[Fe(CN)_6]^{3-}/[Fe(CN)_6]^{4-}$ anodic peak heights on the square root of scan rate. (c) The dependence of 1-N peak on reduction time (300 – 900 s) of GO and (d) concentration of KCl (3 – 100 mM) in reduction solution (red diamond indicates condition selected as optimal; typical DPV voltammograms are shown within insets; arrow is showing trend corresponding to x axis parameter increase). (e) Dependence of 1-N peak on modulation amplitude (5 – 200 mV), (f) modulation time (10 – 100 ms) and (g) speed of polarization (5 – 50 mV · s^{-1}). (h) Dependence of signal on 1-N concentration (0.24 – 31.25 µM).

3.3. ERGO strip microelectrode biosensor

Biosensors based on electrochemical enzymatic activity are promising for numerous diagnostic fields, such as medical screening, food analysis and environmental monitoring (Zhang et al. 2018a; Zhang et al. 2018b). The detection system we used as a proof-of-concept is well documented and is still frequently

used as an ELISA (enzyme-linked immunosorbent assay). The proposed detection mechanism is based on the attachment of immobilization antibody fragment (anti-HT2 (10) Fab) onto the electrode. The coupling was performed *via* carbodiimide chemistry, using EDC/NHS, where the residual carboxylic groups found on the surface of ERGO were crosslinked to the primary amines of the Fab fragment. The anti-IC-HT2 scFv genetically fused with alkaline phosphatase (ALP) is able to recognize the immunocomplex of HT-2 toxin and anti-HT2 (10) Fab. Anti-HT2 (10) Fab is not able to specifically recognize HT-2 from T-2 toxin thus the specificity of analysis was provided by anti-IC-HT2 scFv which shows no cross-reactivity with T-2 and the related molecules (T-2-triol, T-2-tetraol, diacetoxyscirpenol, 15-acetyldeoxynivalenol, 3- acetyldeoxynivalenol, deoxynivalenol, deoxynivalenol-3-glucoside, nivalenol, and neosolaniol) (Arola et al. 2016). ALP is an enzyme which cleaves the phosphate from different molecules with higher efficiency in alkaline conditions. Here non-electroactive 1-NP was used as an ALP substrate. Electroactive product 1-N was produced from 1-NP by ALP (Fig. 4(a)).

Biosensors should be cost-effective and allow for scalable manufacturing. IJP and the use of recombinant fusion antibodies definitely meet these demands. The proposed method of graphene-related material IJP in combination with inkjet-printed tracks (screen-printed here) can dramatically decrease the price of such sensors. The electrochemical reduction seems to be inappropriate since it takes several minutes depending on printed morphology. However the use of a multichannel potentiostat can make this process more time-effective.

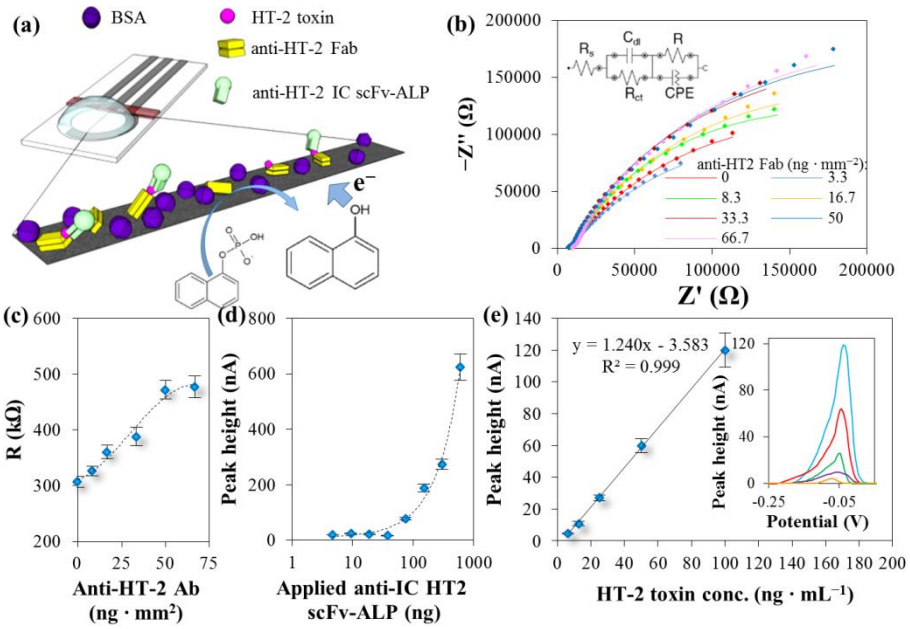

Fig. 4. (a) Scheme of suggested ERGO microelectrode HT-2 toxin biosensor. (b) EIS nyquist plot of ERGO microelectrode modified with different amount of anti-HT-2 Fab (0 – 66.7 ng · mm^{-2}) in 1 mM $[Fe(CN)_6]^{3-}/[Fe(CN)_6]^{4-}$ in 0.1 M KCl and equivalent circuit used for data evaluation in inset. (c) Dependence of R component of EIS equivalent circuit resistance on amount applied anti-HT-2 Fab (0 – 66.7 ng · mm^{-2}). (d) Dependence of suggested biosensor background 1-N signal on amount of applied anti-HT-2 IC scFv-ALP (5 – 600 ng). (e) Dependence of DPV 1-N oxidation signal on concentration of applied HT-2 toxin (6.3 – 100.0 ng · mL^{-1}). Baseline-corrected response (peak) of biosensor to HT-2 toxin at concentration corresponding to calibration curve (inset).

3.4. Application of the designed biosensor

To demonstrate the capabilities of our developed biosensor for possible real-world applications, we have chosen to target the detection of the HT-2 mycotoxin. HT-2 mycotoxins are highly toxic trichothecene mycotoxins produced by *Fusarium* species and have adverse effects on plant products such as wheat, oats and barley, which are all prevalent crops in the European union (Bryla et al. 2018). The harmful effects of HT-2 are manifested not only by inhibition of protein synthesis and cell proliferation in plants, but can also cause acute or chronic intoxication of humans and animals (Rocha et al. 2005). Therefore a

rapid and low-cost detection platform would prove to be advantageous for the health and food safety industry.

The successful attachment of anti-HT2 (10) Fab onto the ERGO working electrode was monitored by electrochemical impedance spectroscopy (EIS). The amount of applied anti-HT2 (10) Fab was transformed into nanogram per square millimeter of working electrodes ($ng \cdot mm^{-2}$). As can be seen in Fig. 4(b), the increasing concentration of attached anti-HT2 (10) Fab resulted in incremental change of the depressed semi-circles in the Nyquist diagram. The impedance measurements were fitted using an equivalent circuit (Fig. 4(b) inset) and the corresponding electronic circuit elements were calculated. The resistive element, labelled in equivalent circuit R, showed increasing trends with increasing amount of applied anti-HT2 (10) Fab (Fig. 4(c)). The amount of applied anti-IC-HT2 scFv-ALP was optimized in order to obtain minimal background response. The same corresponding concentrations of anti-IC-HT2 scFv-ALP were incubated with the anti-HT2 (10) Fab modified electrodes anti-HT2 (10) Fab without introduction of the HT-2 toxin. In our workflow of washing steps, 30 μL of anti-IC-HT2 scFv-ALP ($2.5\ \mu g \cdot mL^{-1}$)~75 ng was selected as the optimal amount of anti-IC-HT2 scFv-ALP added onto the electrode (Fig. 4(d)). Background signal in case of higher anti-IC-HT2 scFv-ALP concentrations substantially increased which is not desirable.

Using optimized conditions, the biosensor was used to determine different concentrations of HT-2 toxin. The response of the biosensor showed increasing DPV 1-N signals with increasing concentrations of HT-2 toxin and showed good linear dependence (Fig. 4(e)) with a limit of detection (LOD) of $1.6\ ng \cdot mL^{-1}$. The low LOD observed is comparable with other methods such as ELISA, surface plasmon resonance biosensors or high-performance liquid chromatography with fluorescence detection (Lippolis et al. 2008; Meneely et al. 2010; Yoshizawa et al. 2004). Khan *et al.* (Khan et al. 2018) reported on a fluorescence resonance energy transfer amplified aptasensor with T-2 toxin (T-2 toxin is rapidly hydrolyzed to HT-2 toxin *in vivo*) with a LOD of $0.93\ pg \cdot mL^{-1}$. Detection limit of $0.38\ ng \cdot mL^{-1}$ was reported for non-competitive immunoassay based on utilization of time-resolved fluorescence resonance

energy transfer (Arola et al. 2016). However, in our case the sensitivity, as well as other detection parameters, can be further tuned by prolonging the incubation times of the substrate with the immobilized ALP (during longer incubation time anti-IC-HT2 scFv-ALP will produce more 1-N). The inset of Fig. 4(e) shows a representative response of the biosensor to 6.3 $ng \cdot mL^{-1}$ of HT-2 toxin. Noticeably, the peak of 1-N shifted from +0.05 V, in the case of 1-N sensing of the bare ERGO microelectrode, to −0.08 V. This shift can be attributed to a change of the pseudoreference electrode potential due to multiple incubation and washing steps. The analytical parameters of HT-2 detection with the proposed system are shown in Tab. 1. Nowadays, ordinary smartphones can be used as complete electrochemical workstations and miniaturized commercial potentiostats are available. Consequently the reported electrode can be used as a part of affordable and portable point-of-need analytical devices beneficial for food quality control and smart farming (da Silva et al. 2017; Vashist et al. 2015). The reported fabrication procedure enables to manufacture the working electrode arrays attractive for analysis multiplexing. Fabrication of such sensors on transparent plastic materials can be beneficial for integration of additional sensing devices with optical readout.

As matrix effects can significantly influence the sensitivity of analysis, an assessment of the matrix effects on the detection of HT-2 were tested using spiked fetal bovine serum (FBS). To determine analytical recovery, one volume of HT-2 standard solution (1 $\mu g \cdot mL^{-1}$) was mixed with 9 volumes of FBS and a blocking buffer in ratio of 1:1. Recovery of the standard ranged from 87.8 to 108.5 % (n = 5).

Tab. 1. Analytical parameters of electrochemical detection of HT-2 toxin.

Substance	Working electrode	Regression equation	Linear dynamic range ($ng \cdot mL^{-1}$)	$R^{2\ a)}$	$LOD^{b)}$ ($ng \cdot mL^{-1}$)
HT-2 toxin	ERGO	y = 1.240x – 3.583	6.3– 100.0	0.999	1.6

a) Regression coefficient; b) LOD (S/N=3).

4. Conclusion

In this study we focused on the fabrication of reduced graphene oxide working electrodes, where reduced graphene was not only the modifier of highly conductive electrode material but also the electrode material itself. We designed and formulated a water-based commercial GO ink that was then used to inkjet print graphene GO, measuring 78 μm in width, onto plasma-treated and chemically etched poly(ethylene 2,6-naphthalate) substrates with screen-printed Ag/AgCl pseudoreference electrode, graphite counter electrode and a graphite working electrode track. The electrochemical reduction of the graphene oxide strip was performed in a KCl solution, where the reduction parameters and electrolyte concentrations were optimized. The successful reduction of the GO was confirmed by Raman spectroscopy, where an increase of D and G peak ratio was observed. The DPV sensing of 1-naphthol with the ERGO microelectrode was optimized with the intention to create an enzymatic electrochemical immunosensor of HT-2 mycotoxin. More precisely, the residual carboxylic groups in ERGO revealed by XPS facilitated the covalent attachment of anti-HT2 (10) Fab via carbodiimide coupling. The presence of analyte in solution was reported by anti-immunocomplex scFv antibody labelled with alkaline phosphatase which produced electroactive 1-naphthol from non-electroactive substrate. The

411 proposed biosensor reached biologically relevant analytical parameters and satisfactory recovery in
412 biological matrix.

413 ## Acknowledgements

414 We acknowledge financial support from EU Graphene Flagship Core 2 Project (No. 785219). This work
415 is also funded by the CERCA Program/Generalitat de Catalunya. ICN2 acknowledges the support of the
416 Spanish MINECO for the Project MAT2017-87202-P and through the Severo Ochoa Centers of
417 Excellence Program under Grant SEV2201320295. Financial support from CEITEC 2020 (LQ1601) is
418 acknowledged. The AFM measurements (GO characterization) performed at Nanobiotechnology Core
419 Facility has been financially supported by Ministry of Education, Youth and Sports of the Czech
420 Republic under the CIISB research infrastructure project LM2015043.
421 The authors wish to express their thanks to Marcos Rosado Iglesias, Elena Del Corro García, Guillaume
422 Sauthier (all Catalan Institute of Nanoscience and Nanotechnology, CSIC and The Barcelona Institute
423 of Science and Technology, Barcelona, Spain) and Jan Přibyl for their expert assistance with SEM,
424 Raman spectroscopy, XPS and AFM analysis, respectively.

425 ## References

426 Arola, H.O., Tullila, A., Kiljunen, H., Campbell, K., Siitari, H., Nevanen, T.K., 2016. Specific Noncompetitive Immunoassay for HT-2 Mycotoxin Detection. Anal. Chem. 88(4),
427 2446-2452.
428 Arola, H.O., Tullila, A., Nathanail, A.V., Nevanen, T.K., 2017. A Simple and Specific Noncompetitive ELISA Method for HT-2 Toxin Detection. Toxins 9(4).
429 Bachmann, B., Adly, N., Schnitker, J., Yakushenko, A., Rinklin, P., Offenhausser, A., Wolfrum, B., 2017. All-inkjet-printed gold microelectrode arrays for extracellular recording
430 of action potentials. Flex. Print. Electron. 2(3).
431 Bartlam, C., Morsch, S., Heard, K.W.J., Quayle, P., Yeates, S.G., Vijayaraghavan, A., 2018. Nanoscale infrared identification and mapping of chemical functional groups on
432 graphene. Carbon 139, 317-324.
433 Benchirouf, A., Muller, C., Kanoun, O., 2016. Electromechanical Behavior of Chemically Reduced Graphene Oxide and Multi-walled Carbon Nanotube Hybrid Material.
434 Nanoscale Res. Lett. 11.
435 Bonaccorso, F., Bartolotta, A., Coleman, J.N., Backes, C., 2016. 2D-Crystal-Based Functional Inks. Adv. Mater. 28(29), 6136-6166.
436 Brownson, D.A.C., Munro, L.J., Kampouris, D.K., Banks, C.E., 2011. Electrochemistry of graphene: not such a beneficial electrode material? RSC Adv. 1(6), 978-988.
437 Bryla, M., Waskiewicz, A., Ksieniewicz-Wozniak, E., Szymczyk, K., Jedrzejczak, R., 2018. Modified Fusarium Mycotoxins in Cereals and Their Products-Metabolism,
438 Occurrence, and Toxicity: An Updated Review. Molecules 23(4).
439 Cammarano, A., De Luca, G., Amendola, E., 2013. Surface modification and adhesion improvement of polyester films. Cent. Eur. J. Chem 11(1), 35-45.
440 Casero, E., Alonso, C., Petit-Dominguez, M.D., Vazquez, L., Parra-Alfambra, A.M., Merino, P., Alvarez-Garcia, S., de Andres, A., Suarez, E., Pariente, F., Lorenzo, E., 2014.
441 Lactate biosensor based on a bionanocomposite composed of titanium oxide nanoparticles, photocatalytically reduced graphene, and lactate oxidase. Microchim. Acta 181(1-2),
442 79-87.
443 Casero, E., Alonso, C., Vazquez, L., Petit-Dominguez, M.D., Parra-Alfambra, A.M., de la Fuente, M., Merino, P., Alvarez-Garcia, S., de Andres, A., Pariente, F., Lorenzo, E.,
444 2013. Comparative Response of Biosensing Platforms Based on Synthesized Graphene Oxide and Electrochemically Reduced Graphene. Electroanalysis 25(1), 154-165.

da Silva, E., Miserere, S., Kubota, L.T., Merkoci, A., 2014. Simple On-Plastic/Paper Inkjet-Printed Solid-State Ag/AgCI Pseudoreference Electrode. Anal. Chem. 86(21), 10531-10534.

da Silva, E., Souto, D.E.P., Barragan, J.T.C., Giarola, J.D., de Moraes, A.C.M., Kubota, L.T., 2017. Electrochemical Biosensors in Point-of-Care Devices: Recent Advances and Future Trends. ChemElectroChem 4(4), 778-794.

Dearden, A.L., Smith, P.J., Shin, D.Y., Reis, N., Derby, B., O'Brien, P., 2005. A low Curing temperature silver ink for use in ink-jet printing and subsequent production of conductive tracks. Macromol. Rapid Commun. 26(4), 315-318.

EC, 2013. Commission Recommendation 2013/165/EU of 27 March 2013 on the presence of T-2 and HT-2 toxin in cereals and cereal products. Off. J. Eur. Commun.(91), 12-15.

Feng, X.Y., Chen, W.F., Yan, L.F., 2016. Electrochemical reduction of bulk graphene oxide materials. RSC Adv. 6(83), 80106-80113.

Gonzalez, E., Barankin, M.D., Guschl, P.C., Hicks, R.F., 2008. Remote Atmospheric-Pressure Plasma Activation of the Surfaces of Polyethylene Terephthalate and Polyethylene Naphthalate. Langmuir 24(21), 12636-12643.

He, P., Derby, B., 2017. Inkjet printing ultra-large graphene oxide flakes. 2D Mater. 4(2).

Hermerschmidt, F., Burmeister, D., Ligorio, G., Pozov, S.M., Ward, R., Choulis, S.A., List-Kratochvil, E.J.W., 2018. Truly Low Temperature Sintering of Printed Copper Ink Using Formic Acid. Adv. Mater. Technol. 3(12).

Hoeng, F., Bras, J., Gicquel, E., Krosnicki, G., Denneulin, A., 2017. Inkjet printing of nanocellulose-silver ink onto nanocellulose coated cardboard. RSC Adv. 7(25), 15372-15381.

Hussein, H.S., Brasel, J.M., 2001. Toxicity, metabolism, and impact of mycotoxins on humans and animals. Toxicology 167(2), 101-134.

Chen, Y., Zhang, X.O., Zhang, D.C., Yu, P., Ma, Y.W., 2011. High performance supercapacitors based on reduced graphene oxide in aqueous and ionic liquid electrolytes. Carbon 49(2), 573-580.

Juang, Z.Y., Wu, C.Y., Lu, A.Y., Su, C.Y., Leou, K.C., Chen, F.R., Tsai, C.H., 2010. Graphene synthesis by chemical vapor deposition and transfer by a roll-to-roll process. Carbon 48(11), 3169-3174.

Kamyshny, A., Magdassi, S., 2014. Conductive Nanomaterials for Printed Electronics. Small 10(17), 3515-3535.

Karim, N., Afroj, S., Malandraki, A., Butterworth, S., Beach, C., Rigout, M., Novoselov, K.S., Casson, A.J., Yeates, S.G., 2017. All inkjet-printed graphene-based conductive patterns for wearable e-textile applications. J. Mater. Chem. C 5(44), 11640-11648.

Kaukoranta, T., Hietaniemi, V., Ramo, S., Koivisto, T., Parikka, P., 2019. Contrasting responses of T-2, HT-2 and DON mycotoxins and Fusarium species in oat to climate, weather, tillage and cereal intensity. Eur. J. Plant Pathol. 155(1), 93-110.

Khan, I.M., Zhao, S., Niazi, S., Mohsin, A., Shoaib, M., Duan, N., Wu, S.J., Wang, Z.P., 2018. Silver nanoclusters based FRET aptasensor for sensitive and selective fluorescent detection of T-2 toxin. Sens. Actuator B-Chem. 277, 328-335.

Kuang, B., Song, W.L., Ning, M.Q., Li, J.B., Zhao, Z.J., Guo, D.Y., Cao, M.S., Jin, H.B., 2018. Chemical reduction dependent dielectric properties and dielectric loss mechanism of reduced graphene oxide. Carbon 127, 209-217.

Kudr, J., Richtera, L., Nejdl, L., Xhaxhiu, K., Vitek, P., Rutkay-Nedecky, B., Hynek, D., Kopel, P., Adam, V., Kizek, R., 2016. Improved Electrochemical Detection of Zinc Ions Using Electrode Modified with Electrochemically Reduced Graphene Oxide. Materials 9(1).

Kuchenbuch, H.S., Becker, S., Schulz, M., Cramer, B., Humpf, H.U., 2018. Thermal stability of T-2 and HT-2 toxins during biscuit- and crunchy muesli-making and roasting. Food Addit. Contam. Part A-Chem. 35(11), 2158-2167.

Li, P.W., Tao, C.A., Wang, B.Y., Huang, J., Li, T.H., Wang, J.F., 2018. Preparation of Graphene Oxide-Based Ink for Inkjet Printing. J. Nanosci. Nanotechnol. 18(1), 713-718.

Lippolis, V., Pascale, M., Maragos, C.M., Visconti, A., 2008. Improvement of detection sensitivity of T-2 and HT-2 toxins using different fluorescent labeling reagents by high-performance liquid chromatography. Talanta 74(5), 1476-1483.

Medina-Sanchez, M., Martinez-Domingo, C., Ramon, E., Merkoci, A., 2014. An Inkjet-Printed Field-Effect Transistor for Label-Free Biosensing. Adv. Funct. Mater. 24(40), 6291-6302.

Meneely, J.P., Sulyok, M., Baumgartner, S., Krska, R., Elliott, C.T., 2010. A rapid optical immunoassay for the screening of T-2 and HT-2 toxin in cereals and maize-based baby food. Talanta 81(1-2), 630-636.

Michel, M., Biswas, C., Kaul, A.B., 2017. High-performance ink-jet printed graphene resistors formed with environmentally-friendly surfactant-free inks for extreme thermal environments. Appl. Mater. Today 6, 16-21.

Paredes, J.I., Villar-Rodil, S., Solis-Fernandez, P., Martinez-Alonso, A., Tascon, J.M.D., 2009. Atomic Force and Scanning Tunneling Microscopy Imaging of Graphene Nanosheets Derived from Graphite Oxide. Langmuir 25(10), 5957-5968.

Park, B.K., Kim, D., Jeong, S., Moon, J., Kim, J.S., 2007. Direct writing of copper conductive patterns by ink-jet printing. Thin Solid Films 515(19), 7706-7711.

Pei, L.M., Li, Y.F., 2017. Rapid and efficient intense pulsed light reduction of graphene oxide inks for flexible printed electronics. RSC Adv. 7(81), 51711-51720.

Raj, M.A., John, S.A., 2013. Fabrication of Electrochemically Reduced Graphene Oxide Films on Glassy Carbon Electrode by Self-Assembly Method and Their Electrocatalytic Application. J. Phys. Chem. C 117(8), 4326-4335.

Ramesha, G.K., Sampath, S., 2009. Electrochemical Reduction of Oriented Graphene Oxide Films: An in Situ Raman Spectroelectrochemical Study. J. Phys. Chem. C 113(19), 7985-7989.

Ren, X., Ma, H.M., Zhang, T., Zhang, Y., Yan, T., Du, B., Wei, Q., 2017. Sulfur-Doped Graphene-Based Immunological Biosensing Platform for Multianalysis of Cancer Biomarkers. ACS applied materials & interfaces 9(43), 37637-37644.

Rocha, O., Ansari, K., Doohan, F.M., 2005. Effects of trichothecene mycotoxins on eukaryotic cells: A review. Food Addit. Contam. Part A-Chem. 22(4), 369-378.

Shiwaku, R., Matsui, H., Nagamine, K., Uematsu, M., Mano, T., Maruyama, Y., Nomura, A., Tsuchiya, K., Hayasaka, K., Takeda, Y., Fukuda, T., Kumaki, D., Tokito, S., 2018. A Printed Organic Circuit System for Wearable Amperometric Electrochemical Sensors. Sci Rep 8.

Singh, M., Haverinen, H.M., Dhagat, P., Jabbour, G.E., 2010. Inkjet Printing-Process and Its Applications. Adv. Mater. 22(6), 673-685.

Stankovich, S., Dikin, D.A., Dommett, G.H.B., Kohlhaas, K.M., Zimney, E.J., Stach, E.A., Piner, R.D., Nguyen, S.T., Ruoff, R.S., 2006. Graphene-based composite materials. Nature 442(7100), 282-286.

Stringer, J., Derby, B., 2009. Limits to feature size and resolution in inkjet printing. J. Eur. Ceram. Soc. 29(5), 913-918.

Su, C.H., Chiu, H.L., Chen, Y.C., Yesilmen, M., Schulz, F., Ketelsen, B., Vossmeyer, T., Liao, Y.C., 2019. Highly Responsive PEG/Gold Nanoparticle Thin-Film Humidity Sensor via Inkjet Printing Technology. Langmuir 35(9), 3256-3264.

Tan, S.M., Ambrosi, A., Chua, C.K., Pumera, M., 2014. Electron transfer properties of chemically reduced graphene materials with different oxygen contents. J. Mater. Chem. A 2(27), 10668-10675.

Toh, S.Y., Loh, K.S., Kamarudin, S.K., Daud, W.R.W., 2014. Graphene production via electrochemical reduction of graphene oxide: Synthesis and characterisation. Chem. Eng. J. 251, 422-434.

Vaseem, M., Lee, K.M., Hong, A.R., Hahn, Y.B., 2012. Inkjet Printed Fractal-Connected Electrodes with Silver Nanoparticle Ink. ACS applied materials & interfaces 4(6), 3300-3307.

Vashist, S.K., Luppa, P.B., Yeo, L.Y., Ozcan, A., Luong, J.H.T., 2015. Emerging Technologies for Next-Generation Point-of-Care Testing. Trends Biotechnol. 33(11), 692-705.

Yang, L.C., Tu, D., Zhao, Z.Y., Cui, J., 2017. Cytotoxicity and apoptosis induced by mixed mycotoxins (T-2 and HT-2 toxin) on primary hepatocytes of broilers in vitro. Toxicon 129, 1-10.

Ye, S.B., Feng, J.C., 2016. The effect of sonication treatment of graphene oxide on the mechanical properties of the assembled films. RSC Adv. 6(46), 39681-39687.

Yoshizawa, T., Kohno, H., Ikeda, K., Shinoda, T., Yokohama, H., Morita, K., Kusada, O., Kobayashi, Y., 2004. A practical method for measuring deoxynivalenol, nivalenol and T-2+HT-2 toxin in foods by an enzyme-linked immunosorbent assay using monoclonal antibodies. Biosci. Biotechnol. Biochem. 68(10), 2076-2085.

Zhan, Z.Y., An, J.N., Wei, Y.F., Tran, V.T., Du, H.J., 2017. Inkjet-printed optoelectronics. Nanoscale 9(3), 965-993.

Zhang, J.L., Yang, H.J., Shen, G.X., Cheng, P., Zhang, J.Y., Guo, S.W., 2010. Reduction of graphene oxide via L-ascorbic acid. Chem. Commun. 46(7), 1112-1114.

Zhang, T., Ma, N., Ali, A., Wei, Q., Wu, D., Ren, X., 2018a. Electrochemical ultrasensitive detection of cardiac troponin I using covalent organic frameworks for signal amplification. Biosens. Bioelectron. 119, 176-181.

Zhang, T., Xing, B., Han, Q.Z., Lei, Y.F., Wu, D., Ren, X., Wei, Q., 2018b. Electrochemical immunosensor for ochratoxin A detection based on Au octahedron plasmonic colloidosomes. Anal. Chim. Acta 1032, 114-121.

Zhong, J.H., Zhang, J., Jin, X., Liu, J.Y., Li, Q.Y., Li, M.H., Cai, W.W., Wu, D.Y., Zhan, D.P., Ren, B., 2014. Quantitative Correlation between Defect Density and Heterogeneous Electron Transfer Rate of Single Layer Graphene. J. Am. Chem. Soc. 136(47), 16609-16617.

Zikulnig, J., Hirschl, C., Rauter, L., Krivec, M., Lammer, H., Riemelmoser, F., Roshanghias, A., 2019. Inkjet printing and characterisation of a resistive temperature sensor on paper substrate. Flex. Print. Electron. 4(1).